Variable Inductor Control Strategy in LCC-S Compensated Wireless Power Transfer Application

Vipinkumar Shriram Meshram
DIEM
University of Salerno
Salerno, Italy
vmeshram@unisa.it

Fabio Corti
DINFO
University of Florence
Firenze, Italy
fabio.corti@unifi.it

Luigi Solimene
DENERG
Politecnico di Torino
Torino, Italy
luigi.solimene@polito.it

Salvatore Musumeci
DENERG
Politecnico di Torino
Torino, Italy
salvatore.musumeci@polito.it

Carlo Stefano Ragusa
DENERG
Politecnico di Torino
Torino, Italy
carlo.ragusa@polito.it

Alberto Reatti
DINFO
University of Florence
Firenze, Italy
alberto.reatti@unifi.it

***Abstract*—This paper presents a control strategy for output voltage regulation of the LCC-S compensated Wireless Power Transfer (WPT) system through a variable inductor. Firstly, the architecture of the system is analyzed, and the relation between the output voltage and the variable inductance is derived. Then, the control strategy that allows to regulate the DC current through the variable inductor to maintain the desired output voltage is presented. Both the steady-state and the dynamic performance of the system are evaluated through Simulink simulations.**

***Index Terms*—Wireless Power Transfer, LCC-S Compensation, Magnetic Control, Variable Inductor.**

I. Introduction

Wireless Power Transfer (WPT) can play a crucial role in the widespread adoption of emerging technologies such as drones [1], electric vehicles [2], and consumer electronics [3]. This technology allows the transmission of electrical power without the need for physical connections. This convenient feature enables smooth charging of devices, electric vehicles, and other electronics, promoting enhanced mobility while eliminating the need for wires [4], [5].

Two main WPT technologies exist, depending on the physical principle: Inductive Wireless Power Transfer (IWPT) and Capacitive Wireless Power Transfer (CWPT) [6], [7]. This paper is focused on Inductive Wireless Power Transfer, a technology that harnesses the magnetic coupling between two coils to transfer electrical power. An alternating current in the first coil, referred to as the transmitter coil or primary coil, generates an alternating magnetic field. This magnetic field induces a voltage in the second coil, known as the receiver coil or secondary coil, which provides the electrical power to charge devices or supply appliances. Since the distance between the coils can be up to tens of centimeters, the coupling coefficient is usually low [8]. For this reason, resonant compensations are usually used to increase conversion efficiency. One of the most promising compensations is the LCC-S [9]. This compensation can maintain stable operation over a wide range of load conditions. The resonant topology allows for better control of power delivery, ensuring a smooth transition between different load levels. In addition, it results in lower voltage stress on switching devices and other components, which can extend their lifespan and improve the overall reliability of the converter [10].

Different dynamic control strategies have been presented for this topology. The most widely used consists of the Pulse Frequency Modulation (PFM) where the operating frequency is regulated to match the resonance of the transmitter and receiver coils [11]. By adjusting the operating frequency, the system can optimize power transfer efficiency and adapt to changes in load conditions [12]. Another approach is the Pulse Width Modulation (PWM) where, by modulating the width of the switching pulses, the average output voltage and current are regulated, allowing for precise control of power delivery to the load [13].

In this paper, attention is focused on the Magnetic Control (MC) of the LCC-S compensation. This control consists of exploiting the magnetic saturation of the resonant topology inductor [14]. In fact, by changing the value of the inductance, it is possible to regulate the power transferred to the load [15]. This variation is obtained by designing the inductor with an additional coil where ad DC current is flowing. Changing the value of the DC current it is possible to change the point of working along the B-H curve of the material [16]. The principle of operation of the converter has been widely proven in [14]. Anyway, the dynamic control of the system is actually missing in the literature.

For this reason, this paper proposes the dynamic control of the LCC-S compensation by magnetic control. Both the steady-state and transient performance are evaluated in a Matlab-Simulink environment.

The paper is organized as follows. In Section II, the analytical analysis of the LCC-S compensation is presented. In

978-88-87237-60-3

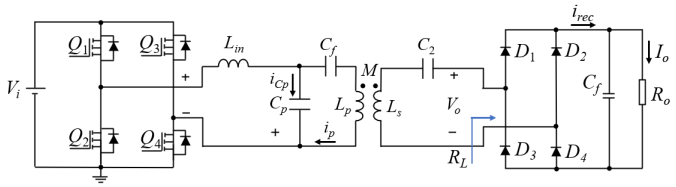

Fig. 1. LCC-S compensation topology.

Section III, the magnetic control is introduced. In Section IV, the proposed dynamic control is presented. In Section V, the simulation results are shown. In Section VI, the conclusions are derived.

II. LCC-S Compensation

The circuit of the LCC-S compensation is shown in Fig. 1. To operate in resonance, the reactive components are designed as [17]:

$$C_{\mathrm{p}} = \frac{1}{\omega^2 L_{\mathrm{in}}}, \tag{1}$$

$$C_{\mathrm{f}} = \frac{1}{\omega^2 \left(L_{\mathrm{p}} - L_{\mathrm{in}}\right)}, \tag{2}$$

$$C_s = \frac{1}{\omega^2 L_{\mathrm{s}}}. \tag{3}$$

The characteristics of the system studied in this paper are summarized in Table I.

TABLE I
System Costraints

Parameter	Value	Description
f_{s}	85 kHz	Operating frequency
V_{I}	48 V	DC input voltage
P_{o}	200 W	Output power
k	0.2	Coupling coefficient
L_{P}	80 μH	Primary coil inductance
R_{p}	0.1 Ω	Primary coil parasitic resistance
L_{s}	80 μH	Secondary coil inductance
R_{s}	0.1 Ω	Secondary coil parasitic resistance
R_{L}	50 Ω	Load resistance

Using (1), (2) and (3) and the design procedure presented in [17], the values of the components shown in Table II are obtained.

TABLE II
Compensation Network Specifications

Parameter	Value	Description
C_{f}	47.9 nF	Filter capacitor
L_{in}	6.9 μH	Input inductor
C_{p}	50.8 nF	Primary capacitor
C_{s}	43.8 nF	Secondary capacitor

Using the Kirchhoff Voltage Law (KVL) and Kirchhoff Current Law (KCL), the output power P_{o} and the efficiency η can be calculated as

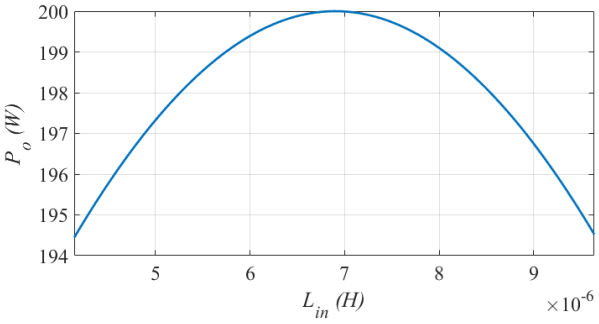

Fig. 2. Variation of the output power with respect to the inductance L_{in}.

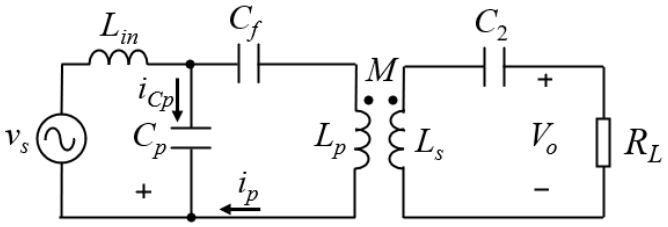

Fig. 3. Equivalent electric circuit of LCC-S compensation.

$$P_{\mathrm{o}} = \frac{V_{\mathrm{s}}^2 M^2 R_{\mathrm{L}}}{\left[\left(\frac{R}{\omega^2 C_{\mathrm{p}}} - \delta\left(\beta C_{\mathrm{p}} R_{\mathrm{p}} + \gamma R C_{\mathrm{p}}\right)\right)^2 + \left(\frac{\beta}{\omega^2 C_{\mathrm{p}}} + \delta\left(C_{\mathrm{p}} K_2 - C_{\mathrm{p}}\gamma\beta\right)\right)^2\right]}, \tag{4}$$

and

$$\eta = \frac{P_{\mathrm{out}}}{\frac{V_{\mathrm{S}}^2}{a^2+b^2}\left(K_2 a - \gamma\beta a + b\gamma R + \beta R_{\mathrm{P}}\right)}, \tag{5}$$

where $a = \frac{R}{\omega^2 C_{\mathrm{P}}^2} - \beta R_{\mathrm{P}}\delta - \delta\gamma R$, $b = \frac{\beta}{\omega^2 C_{\mathrm{P}}^2} + \delta K_2 - \delta\gamma\beta$, $R = R_{\mathrm{L}} + R_{\mathrm{s}}$, $\delta = \omega L_{\mathrm{in}} - \frac{1}{\omega C_{\mathrm{P}}}$, $\gamma = \omega L_{\mathrm{P}} - \frac{1}{\omega C_{\mathrm{P}}} - \frac{1}{\omega C_{\mathrm{f}}}$, $\beta = \omega L_{\mathrm{s}} - \frac{1}{\omega C_{\mathrm{s}}}$, and $M = k\sqrt{L_{\mathrm{P}} L_{\mathrm{s}}}$.

The steady-state variation of the output power with respect to the inductance variation is shown in Fig. 2. As can be seen, the maximum power corresponds to the nominal value of the inductance. Then, by increasing or decreasing the inductance L_{in}, it is possible to reduce the power delivered to the load. This is substantially the principle of operation of the proposed control strategy.

A. Small-Signal Model

Applying the First Harmonic Analysis (FHA) to the equivalent circuit shown in Fig. 3, the expression of the output voltage in the Laplace domain can be obtained.

Isolating the term L_{in}, the relationship between output voltage $V_{\mathrm{o}}(s)$ and the input inductance L_{in} can be expressed by:

$$V_{\mathrm{o}}(s) = \frac{k_1(s)}{k_2(s) + k_3(s) L_{\mathrm{in}}}, \tag{6}$$

where the expression of k_1(s), k_2(s) and k_3(s) are shown in the Appendix.

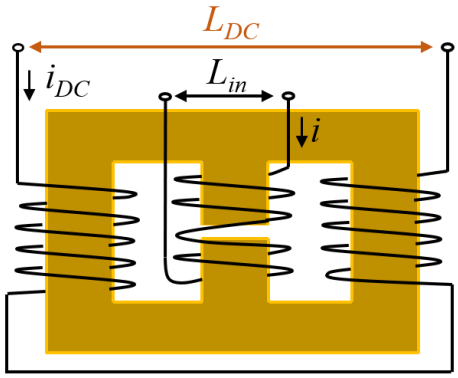

Fig. 4. Variable inductor architecture.

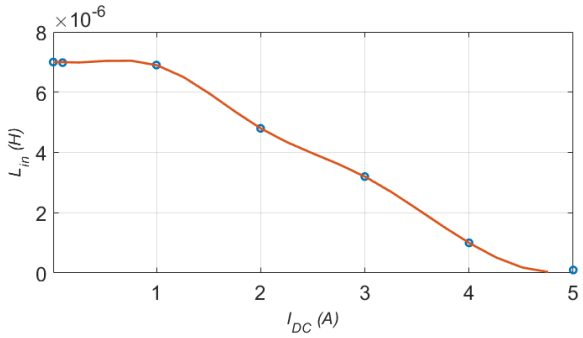

Fig. 5. Variation of the resonant inductance L_{in} as a function of the DC current i_{DC}

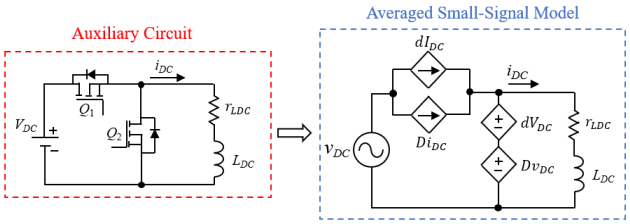

Fig. 6. Auxiliary circuit equivalent circuit.

III. Variable Inductor Design and Auxiliary Circuit Modeling

A. Variable Inductor Design

The structure of the variable inductance is shown in Fig. 4.

A controlled variable inductor (CVI) operates by managing the differential inductance of the component via an auxiliary magnetizing winding that receives power from a DC current source. The underlying concept of a CVI revolves around modifying the differential permeability of a magnetic material, defined as

$$\mu_{\mathrm{d}} = \frac{1}{\mu_0}\frac{\mathrm{d}B}{\mathrm{d}H}. \tag{7}$$

At low levels of the applied magnetizing current, and thus magnetic field, the material functions within a linear region of the magnetization curve, resulting in a nearly constant differential permeability profile. As the magnetic field strength increases, the material transitions towards the roll-off region of the magnetization curve. Here, the differential permeability rapidly declines, ultimately approaching the saturation region, where the minimum value of the permeability is achieved.

Thus the differential inductance can be directly related to the differential permeability of the core:

$$L_{\mathrm{d}} = N^2\frac{S}{l_{\mathrm{fe}}}\frac{\mathrm{d}B}{\mathrm{d}H} = N^2\frac{S}{l_{\mathrm{fe}}}\,\mu_0\,\mu_{\mathrm{d}}. \tag{8}$$

Following the procedure presented in [14], the variation of inductance shown in Fig. 5 is obtained.

B. Auxiliary Circuit Small-Signal Modeling

As previously explained, a DC current is required to regulate the variable inductance, as shown in Fig. 5. For the current regulation i_{DC}, an auxiliary circuit is used. In this paper, an H-bridge connected with a DC voltage is used to regulate the magnetizing current of the variable inductor. A schematic is shown in Fig. 6.

To perform the dynamic control, different modeling approaches are available in the literature [20]. Using the approach presented in [21], the averaged large-signal model can be obtained as shown in Fig. 6. Applying the KCL and KVL, one obtains:

$$Dv_{\mathrm{DC}} + V_{\mathrm{DC}}d = \left(r_{\mathrm{LDC}} + sL_{\mathrm{DC}}\right)i_{\mathrm{DC}}. \tag{9}$$

The transfer function that relates the variation of the DC current when a variation of duty cycle occurs can be calculated assuming v_{DC} = 0. Thus, the output current to duty cycle transfer function can be calculated as

$$P_1(s) = \frac{i_{\mathrm{DC}}}{d} = \frac{V_{\mathrm{DC}}}{r_{\mathrm{LDC}} + sL_{\mathrm{DC}}}. \tag{10}$$

C. System Control Strategy

The schematic of the proposed output voltage control strategy is shown in Fig. 7. The output voltage v_{o} is compared with a reference voltage $v_{\mathrm{o}}^{\mathrm{r}}$ and an error e_{v} is generated. This error is used to control the duty cycle of the half-bridge

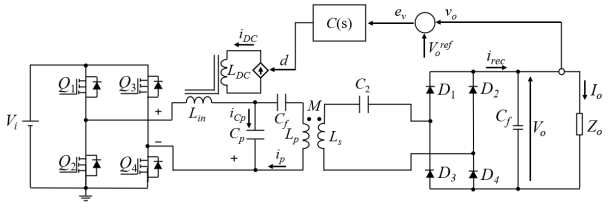

Fig. 7. System control schematic.

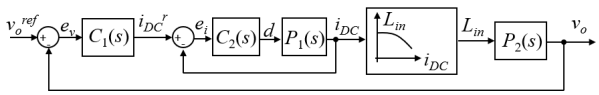

Fig. 8. Block diagram of the control strategy.

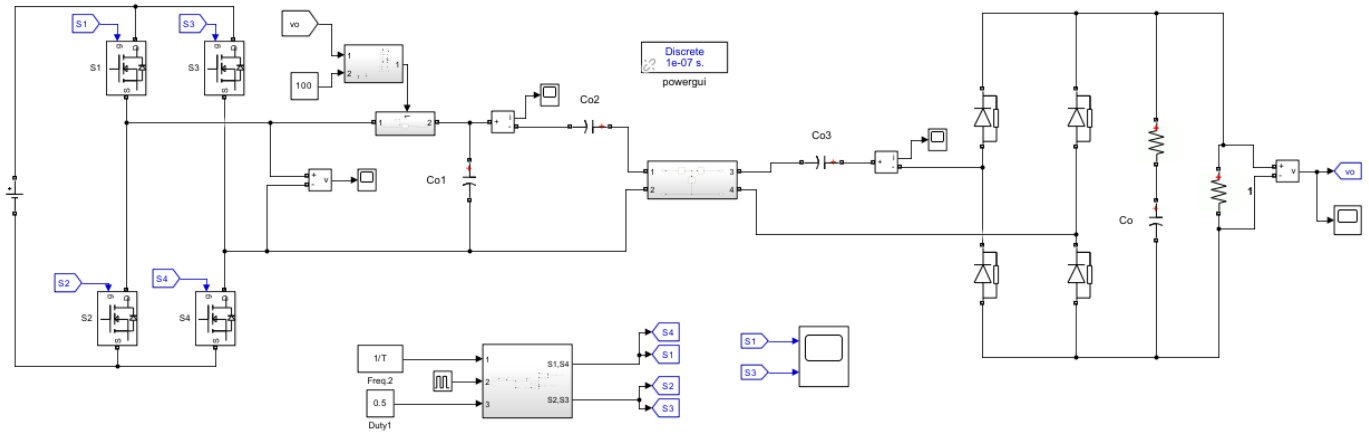

Fig. 9. Simulink schematic.

inside the auxiliary circuit shown in Fig. 6 in order to change the DC current i_{DC} flowing through the variable inductance L_{in}. This is performed by a PID controller $C_2(\mathrm{s})$, tuned using the PID Tuner Matlab tool. The block diagram of the control strategy is shown in Fig. 8. The variation of duty cycle d of the circuit in Fig. 6 is mapped into a variation of DC current i_{DC} by the voltage transfer function $P_1(s)$. Then, the DC current is mapped to a variation of inductance by a lookup table, using the characteristics of the variable inductor shown in Fig. 5. The current value of inductance is used to compute the corresponding variation output voltage using (6).

IV. Simulation Results

A MATLAB-Simulink simulation has been performed to validate the proposed control strategy, as shown in Fig. 9. In Fig. 10, the principle of operation of the auxiliary circuit is evaluated. As it can be seen, the reference of the inductor DC current i_{DC} is varied with 2A steps (red trace). The control system is able to properly follow the desired value of current (blue trace) by varying the duty cycle of the converter (green trace). Then, by increasing the value of the DC current, a reduction of the inductance occurs. This allows for output voltage regulation, as shown in the brown trace of the last plot.

In Fig. 11, the transient of the output voltage is shown. As can be seen, the proposed controller allows for the desired value of output voltage to be followed.

In Fig. 12, the primary current i_{p} and the secondary current i_{s} in steady state condition are shown. Finally, the DC-DC conversion efficiency has been evaluated by varying the output power by increasing the DC current. The results are shown in Fig. 13. As expected, the maximum efficiency is obtained at the nominal output power $P_{\mathrm{o}} = 200$ W, since the system operates in resonance and the reactive power circulating is minimized. At the nominal operating condition, i.e. $P_{\mathrm{o}} = 200$ W, the contributions to the losses are subdivided as shown in Fig. 14. As can be seen, most of the losses are due to the primary inverter and the rectifier. Considerable contributions

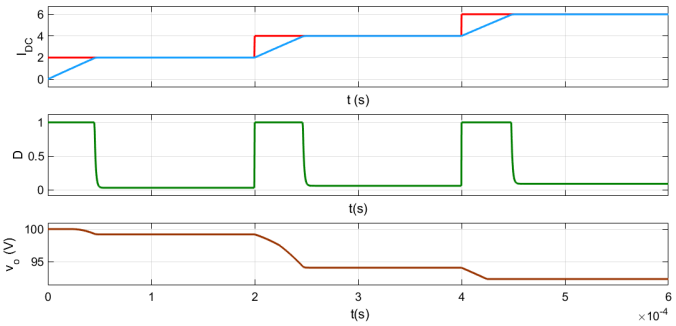

Fig. 10. Simulink simulation results. Blue trace: auxiliary circuit DC current i_{DC}. Green trace: duty cycle d. Brown trace: output voltage v_{o}

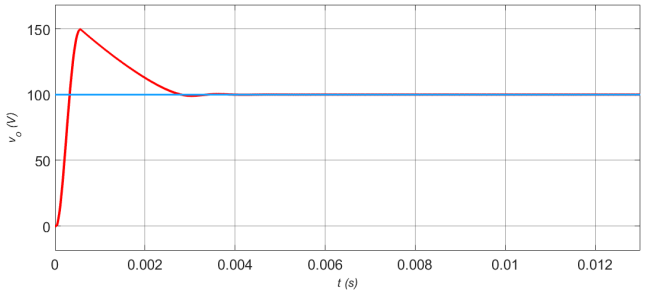

Fig. 11. Output voltage transient.

are also due to the parasitic resistance on the primary and secondary sides. A minor contribution is due to the auxiliary circuit. In Fig. 15, the same analysis has been performed at $P_{\mathrm{o}} = 180$ W. In this case, the current flowing through the DC branch of the variable inductor increases, leading to higher power losses. Anyway, since the current flows through a low resistance, i.e. $r_{\mathrm{DC}} = 0.1\ \Omega$, the contribution to the losses of the auxiliary circuit is, in any case, reduced.

V. Conclusions

This paper evaluates the dynamic performance of a control strategy for an LCC-S wireless power transfer system. A

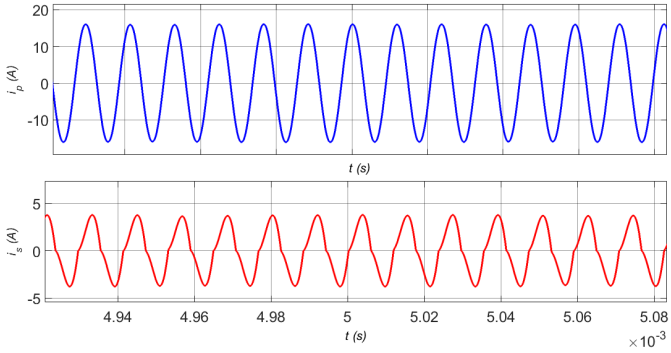

Fig. 12. Primary (blue trace) and secondary current (red trace).

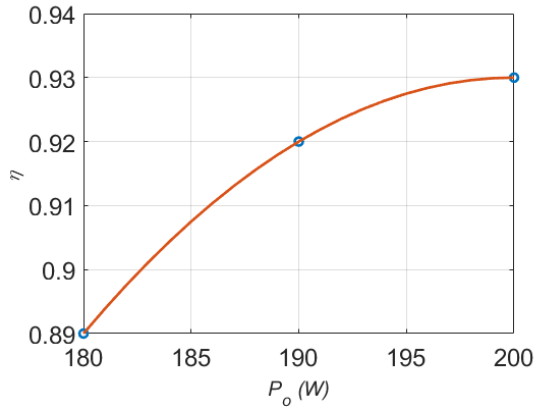

Fig. 13. DC-DC system efficiency, including the power losses of the auxiliary circuit at different output power.

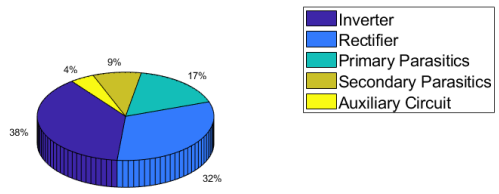

Fig. 14. Contributions of power losses at the nominal operating condition $P_o = 200$ W.

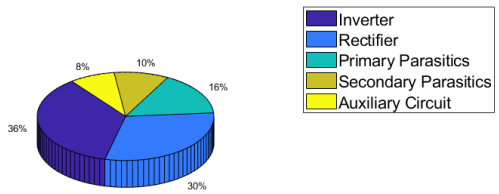

Fig. 15. Contributions of power losses at the nominal operating condition $P_o = 180$ W.

simplified transfer function for the auxiliary circuit has been derived and integrated into the control strategy. A steady-state analysis focused on the evaluation of the efficiency at different operating conditions has been carried out, and the contribution of the auxiliary circuit to the power losses has been analyzed. The results obtained highlight the good performance of the proposed control strategy. As future developments, a more accurate model based on an extended describing function will be used to model the LCC-S compensation to improve the control performance.

Appendix

The coefficients of the LCC-S output voltage transfer function are

$$\begin{aligned} k_1(s) =& C_2C_fMR_LV_ss^3 \\ & \cdot (C_2R_Ls + (C_2L_2 + C_fL_1)s^2 \\ & + (C_2C_fL_1R_L - C_2C_fM^2)s^4 + 1), \end{aligned} \tag{11}$$

$$\begin{aligned} k_2(s) =& s^2(C_f + C_p + C_sC_fL_ss^2 + C_sC_pL_ss^2 + \\ & + C_fC_pL_ps^2 + C_sC_fR_Ls + C_sC_pR_Ls + \\ & - C_sC_fC_pM^2s^4 + C_sC_fC_pL_pL_ss^4 + \\ & + C_sC_fC_pL_pR_Ls^3) \\ & \cdot (C_sR_Ls + C_sL_ss^2 + C_fL_ps^2 + \\ & + C_fMs^2 - 2C_sC_fM^2s^4 \\ & + C_sC_fL_pL_ss^4 + C_sC_fL_sMs^4 + \\ & + C_sC_fL_pR_Ls^3 + C_sC_fMR_Ls^3 + 1), \end{aligned} \tag{12}$$

and

$$\begin{aligned} k_3(s) =& C_s^2C_f^2L_p^2L_s^2s^8 + 2C_s^2C_f^2L_p^2L_sR_Ls^7 + \\ & + C_s^2C_f^2L_p^2R_L^2s^6 + C_s^2C_f^2L_pL_s^2Ms^8 \\ & - 3C_s^2C_f^2L_pL_sM^2s^8 + 2C_s^2C_f^2L_pL_sMR_Ls^7 + \\ & - 3C_s^2C_f^2L_pM^2R_Ls^7 + C_s^2C_f^2L_pMR_L^2s^6 + \\ & - C_s^2C_f^2L_sM^3s^8 + 2C_s^2C_f^2M^4s^8 + \\ & - C_s^2C_f^2M^3R_Ls^7 + 2C_s^2C_fL_pL_s^2s^6 + \\ & + 4C_s^2C_fL_pL_sR_Ls^5 + 2C_s^2C_fL_pR_L^2s^4 + \\ & + C_s^2C_fL_s^2Ms^6 - 3C_s^2C_fL_sM^2s^6 + \\ & + 2C_s^2C_fL_sMR_Ls^5 - 3C_s^2C_fM^2R_Ls^5 + \\ & + C_s^2C_fMR_L^2s^4 + C_s^2L_s^2s^4 + \\ & + 2C_s^2L_sR_Ls^3 + C_s^2R_L^2s^2 + \\ & + 2C_sC_f^2L_p^2L_ss^6 + 2C_sC_f^2L_p^2R_Ls^5 + \\ & + 2C_sC_f^2L_pL_sMs^6 - 3C_sC_f^2L_pM^2s^6 + \\ & + 2C_sC_f^2L_pMR_Ls^5 - C_sC_f^2M^3s^6 + \\ & + 4C_sC_fL_pL_ss^4 + 4C_sC_fL_pR_Ls^3 + \\ & + 2C_sC_fL_sMs^4 - 3C_sC_fM^2s^4 + \\ & + 2C_sC_fMR_Ls^3 + 2C_sL_ss^2 + \\ & + 2C_sR_Ls + C_f^2L_p^2s^4 + \\ & + C_f^2L_pMs^4 + 2C_fL_ps^2 + C_fMs^2 + 1. \end{aligned} \tag{13}$$

REFERENCES

[1] J. Zhou, B. Zhang, W. Xiao, D. Qiu and Y. Chen, "Nonlinear Parity-Time-Symmetric Model for Constant Efficiency Wireless Power Transfer: Application to a Drone-in-Flight Wireless Charging Platform," in IEEE Transactions on Industrial Electronics, vol. 66, no. 5, pp. 4097-4107, May 2019, doi: 10.1109/TIE.2018.2864515.

[2] F. Corti et al., "A Low-Cost Secondary-Side Controlled Electric Vehicle Wireless Charging System using a Full-Active Rectifier," 2018 International Conference of Electrical and Electronic Technologies for Automotive, Milan, Italy, 2018, pp. 1-6, doi: 10.23919/EETA.2018.8493165.

[3] H. Hoang, S. Lee, Y. Kim, Y. Choi and F. Bien, "An adaptive technique to improve wireless power transfer for consumer electronics," in IEEE Transactions on Consumer Electronics, vol. 58, no. 2, pp. 327-332, May 2012, doi: 10.1109/TCE.2012.6227430.

[4] L. Pugi et al. , "Application of Wireless Power Transfer to Railway Parking Functionality: Preliminary Design Considerations with Series-Series and LCC Topologies", Journal of Advanced Transportation, Volume 2018, Article number 8103140, DOI 10.1155/2018/8103140.

[5] Li, Weijie, Lijun Diao, Weiyao Mei, Zhonghao Dongye, Xuqing Qin, and Zheming Jin. 2023. "Optimized Resonant Network Design for High Energy Transfer Efficiency of the WPT System" Electronics 12, no. 9: 1984. https://doi.org/10.3390/electronics12091984

[6] Wang Z, Zhang Y, He X, Luo B, Mai R. "Research and Application of Capacitive Power Transfer System: A Review". Electronics. 2022; 11(7):1158. https://doi.org/10.3390/electronics11071158

[7] Dariusz Czarkowskiet al, "Zero Voltage Switching Condition in Class-E Inverter for Capacitive Wireless Power Transfer Applications", Energies 14, no. 4: 911, 2021, https://doi.org/10.3390/en14040911

[8] Abou Houran, Mohamad, Xu Yang, and Wenjie Chen. 2018. "Magnetically Coupled Resonance WPT: Review of Compensation Topologies, Resonator Structures with Misalignment, and EMI Diagnostics" Electronics 7, no. 11: 296. https://doi.org/10.3390/electronics7110296

[9] S. Jayalath and A. Khan, "Design, Challenges, and Trends of Inductive Power Transfer Couplers for Electric Vehicles: A Review," in IEEE Journal of Emerging and Selected Topics in Power Electronics, vol. 9, no. 5, pp. 6196-6218, Oct. 2021, doi: 10.1109/JESTPE.2020.3042625.

[10] F. Corti, A. Reatti, G. Patrizi, L. Ciani, M. Catelani, M.K. Kazimierczuk, "Probabilistic evaluation of power converters as support in their design", IET Power Electronics, Volume 13, Issue 19, Pages 4542 - 4550, December 2020, DOI 10.1049/iet-pel.2020.0828

[11] Z. Hua, K. T. Chau, W. Liu and X. Tian, "Pulse Frequency Modulation for Parity-Time-Symmetric Wireless Power Transfer System," in IEEE Transactions on Magnetics, vol. 58, no. 8, pp. 1-5, Aug. 2022, Art no. 8002005, doi: 10.1109/TMAG.2022.3153499.

[12] Tang, Li-Chuan, Shyr-Long Jeng, Edward-Yi Chang, and Wei-Hua Chieng. 2021. "Variable-Frequency Pulse Width Modulation Circuits for Resonant Wireless Power Transfer" Energies 14, no. 12: 3656. https://doi.org/10.3390/en14123656

[13] P. M. -Y. Fan and M. H. bin Mohd Daut, "Near-Unity Power Factor, Voltage Step-Up/Down Conversion Pulse-Width Modulated Switching Rectification for Wireless Power Transfer Receiver," in IEEE Transactions on Power Electronics, vol. 34, no. 11, pp. 10960-10969, Nov. 2019, doi: 10.1109/TPEL.2019.2900276.

[14] L. Solimene, F. Corti, S. Musumeci, C. S. Ragusa, A. Reatti, E. Cardelli, "Design and modelling of a controlled saturable inductor for an LCC-S compensated WPT system", Journal of Magnetism and Magnetic Materials, Volume 564, Part 2, 2022, https://doi.org/10.1016/j.jmmm.2022.170056.

[15] L. Solimene, F. Corti, S. Musumeci, A. Reatti and C. S. Ragusa, "A controlled variable inductor for an LCC-S compensated Wireless Power Transfer system," IECON 2022 – 48th Annual Conference of the IEEE Industrial Electronics Society, Brussels, Belgium, 2022, pp. 1-6, doi: 10.1109/IECON49645.2022.9968576.

[16] L. Solimene, F. Corti, S. Musumeci, C. S. Ragusa and A. Reatti, "Magnetic Control of LCC-S Compensated Wireless Power Transfer System," 2022 International Symposium on Power Electronics, Electrical Drives, Automation and Motion (SPEEDAM), Sorrento, Italy, 2022, pp. 160-165, doi: 10.1109/SPEEDAM53979.2022.9842241.

[17] J. Yang, X. Zhang, K. Zhang, X. Cui, C. Jiao and X. Yang, "Design of LCC-S Compensation Topology and Optimization of Misalignment Tolerance for Inductive Power Transfer," in IEEE Access, vol. 8, pp. 191309-191318, 2020, doi: 10.1109/ACCESS.2020.3032563.

[18] W. Wang, J. Deng, D. Chen, Z. Wang and S. Wang, "A Novel Design Method of LCC-S Compensated Inductive Power Transfer System Combining Constant Current and Constant Voltage Mode via Frequency Switching," in IEEE Access, vol. 9, pp. 117244-117256, 2021, doi: 10.1109/ACCESS.2021.3105103.

[19] J. Lu, G. Zhu, H. Wang, F. Lu, J. Jiang and C. C. Mi, "Sensitivity Analysis of Inductive Power Transfer Systems With Voltage-Fed Compensation Topologies," in IEEE Transactions on Vehicular Technology, vol. 68, no. 5, pp. 4502-4513, May 2019, doi: 10.1109/TVT.2019.2903565.

[20] F. . -S. Tsai, "Small-signal and transient analysis of a zero-voltage-switched, phase-controlled PWM converter using averaged switch model," in IEEE Transactions on Industry Applications, vol. 29, no. 3, pp. 493-499, May-June 1993, doi: 10.1109/28.222417.

[21] A. Ayachit and M. K. Kazimierczuk, "Averaged Small-Signal Model of PWM DC-DC Converters in CCM Including Switching Power Loss," in IEEE Transactions on Circuits and Systems II: Express Briefs, vol. 66, no. 2, pp. 262-266, Feb. 2019, doi: 10.1109/TCSII.2018.2848623.